MIT Open Access Articles

Effects of Surface Waviness on Fan Blade Boundary Layer Transition and Profile Loss— Part I: Methodology and Computational Results

Massachusetts Institute of Technology

Jinwook Lee[1,2]
Gas Turbine Laboratory,
Department of Aeronautics and Astronautics,
Massachusetts Institute of Technology,
Cambridge, MA 02139
e-mails: jinwook@mit.edu;
jinwook.lee@spacex.com

Zoltán S. Spakovszky
Gas Turbine Laboratory,
Department of Aeronautics and Astronautics,
Massachusetts Institute of Technology,
Cambridge, MA 02139
e-mail: zolti@mit.edu

Edward M. Greitzer
Gas Turbine Laboratory,
Department of Aeronautics and Astronautics,
Massachusetts Institute of Technology,
Cambridge, MA 02139
e-mail: greitzer@mit.edu

Mark Drela
Gas Turbine Laboratory,
Department of Aeronautics and Astronautics,
Massachusetts Institute of Technology,
Cambridge, MA 02139
e-mail: drela@mit.edu

Jérôme Talbotec
Safran Aircraft Engines Etablissement de
Villaroche sud Rond-point René Ravaud - Réau,
Moissy-Cramayel CEDEX 77550, France
e-mail: jerome.talbotec@safrangroup.com

Effects of Surface Waviness on Fan Blade Boundary Layer Transition and Profile Loss—Part I: Methodology and Computational Results

This two-part paper describes a new approach to determine the effect of surface waviness, arising from manufacture of composite fan blades, on transition onset location movement and hence fan profile losses. The approach includes analysis and computations of unsteady disturbances in boundary layers over a wavy surface, assessed and supported by wind tunnel measurements of these disturbances and the transition location. An integrated framework is developed for analysis of surface waviness effects on natural transition. The framework, referred to as the extended e^N method, traces the evolution of disturbance energy transfer in flow over a wavy surface, from external acoustic noise through exponential growth of Tollmien–Schlichting (TS) waves, to the start and end of the transition process. The computational results show that surface waviness affects the transition onset location due to the interaction between the surface waviness and the TS boundary layer instability and that the interaction is strongest when the geometric and TS wavelengths match. The condition at which this occurs, and the initial amplitude of the boundary layer disturbances that grow to create the transition onset is maximized, is called receptivity amplification. The results provide first-of-a-kind descriptions of the mechanism for the changes in transition onset location as well as quantitative calculations for the effects of surface waviness on fan performance due to changes in surface wavelength, surface wave amplitude, and the location at which the waviness is initiated on the fan blade. [DOI: 10.1115/1.4052235]

Keywords: boundary layer instability, natural transition, receptivity, computational fluid dynamics (CFD), fan aerodynamic design

1 Introduction

1.1 Background to the Problem. Fabrication of carbon composite aeroengine fan blades involves the application of resin over a woven carbon fiber matrix. The blade surface that results has small amplitude waviness, with geometric wavelengths set by the fiber matrix configuration and typically on the order of a few percent of the chord. The geometric surface wave amplitude is on the order of 10^{-5} of the chord.

The surface waviness has been suspected to cause an aerodynamic loss that is larger than that in a nominally equivalent metal blade with a non-wavy surface because waviness moves the location of boundary layer transition, from laminar to turbulent flow, upstream, resulting in a larger region of turbulent boundary layer flow and thus increased loss. In this two-part paper, we explain the physical mechanism responsible for the change in transition onset due to waviness, present a new methodology for quantitative estimates of this change, describe a series of experiments that support the proposed conceptual framework, and propose guidelines, based on the concepts, to improve the aerodynamic performance of blading with surface waviness.

There has been a large amount of research on transition to turbulence on turbomachinery blades, but the problem addressed here

breaks different ground from almost all that work, in at least two important aspects. First, in blading within engine cores (compressors and turbines as contrasted with fans), there are impinging turbulent wakes from upstream. As described for example in Refs. [1,2], the transition process in this situation, referred to as *bypass transition* in the literature [3] is strongly linked to the movement of these wakes through the downstream blade passage. For civil fans, however, there are no upstream blade rows. The transition process, referred to as *natural transition,* thus has a different series of physical features. Natural transition is a process triggered by two-dimensional Tollmien–Schlichting (TS) boundary layer instability waves, which evolve to three-dimensional waves, creation and breakdown of three-dimensional vortical structures, formation of turbulent spots, and fully turbulent flow, as reviewed in Ref. [4].

Second, the external disturbances which trigger the boundary layer instabilities that lead to transition are acoustic, rather than vortical, as they are in bypass transition for embedded blading, and the external disturbance wavelengths encountered are many times the blade geometric wavelength [3]. As such there needs to be a specific mechanism that both (i) couples the external length scales to the boundary layer instability waves, which are typically much shorter, and (ii) sets the initial amplitude of the waves. The initial amplitude is determined by *boundary layer receptivity*, the energy transfer from disturbances in the freestream that "enter the boundary layer as steady and/or unsteady fluctuations of the basic state" [5]. Receptivity can be categorized as vortical or acoustic [5], but for fan blades at cruise, with freestream turbulence intensity less than 0.1% [6], the acoustic receptivity determines the initial disturbance amplitude [7–9]. We will show how this phenomenon, which has not

been previously addressed for fan blade flow, can be coupled with surface geometry of carbon composite fan blade and governs a new loss mechanism.

In addition to these two major differences between fan and core boundary layer transition, there is also an important differentiation with much previous work on transition to turbulence, namely that between waviness and roughness. Surface roughness, which is of different scale in length compared to waviness by orders of magnitude, has been investigated extensively (see Ref. [10] for a comprehensive review of the topic). In contrast, there is a limited literature on the effect of waviness. Although there has been recent efforts towards characterizing the waviness effect on compressor performance [11], the mechanisms were not relevant to carbon composite fan blades due to different length scales examined.

1.2 Hypothesis and Scope of the Paper. The specific issue we address is the effect of waviness on natural transition and aerodynamic loss in aeroengine civil fans. The research objectives are to

(1) define the aerodynamic regimes and geometric conditions under which surface waviness is detrimental to fan performance and quantify the possible performance losses,
(2) determine the relevant mechanisms such that we can scale the results, and thus estimate loss, for other surface waviness configurations and aerodynamic operation,
(3) define the opportunities for increases in performance in blades with surface waviness and the actions needed to achieve these increases.

The focus of the work can be stated in terms of a hypothesis about the physical mechanism: (i) surface waviness affects fan performance through movement of the natural transition location; (ii) this movement is determined by amplification of boundary layer disturbances, specifically Tollmien–Schlichting (TS) instability waves, due to resonance between the TS waves and the surface geometric wavelength.

Part I of the paper focuses on the development of a new methodology which stems from the above hypothesis. In the next section we describe the overall approach including geometric regimes and physical mechanisms. We then present an outline of the new methodology and introduce basic ideas of boundary layer disturbance receptivity. Following that, the approach is described in detail, first the disturbance wave growth that leads to transition onset, then the criteria for onset as well as transition end. The last section presents application of the methodology for different parameters: pressure gradients, acoustic disturbances, and surface roughness, to show the magnitude of changes that can be encountered in practice.

Part II describes the assessment of the hypothesis against experiments, in a wind tunnel designed to carry out measurements of transition behavior, using hot wires and infrared thermography. It also includes estimates of loss variation, which can be up to 1% in isentropic efficiency, as a function of fan aerodynamic parameters and basic guidelines for increasing efficiency of wavy blades. The overarching finding is that the experiments, which are consistent with the hypothesis and in quantitative agreement with the analysis and other parts of the Part I methodology, show the utility of the methodology that is proposed.

2 Fan Blade Natural Transition: Physical Processes and Geometric Regimes

2.1 Elements of Transition Process. Figure 1 gives a pictorial description of flow phenomena in natural transition. The figure shows an external acoustic disturbance impinging on a boundary layer over a wavy wall and lists the different elements that characterize the stages along a fan blade. Stages 1, 2, and 3 can be described as linear processes; stages 4 and 5 are non-linear.
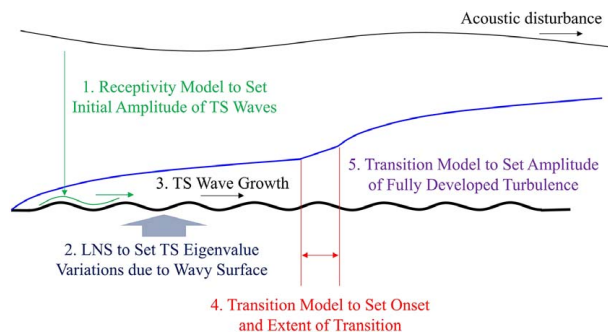
Fig. 1 Elements of the natural transition process

Element 1 is receptivity, the coupling of external disturbances, such as sound or vorticity, to the disturbances in the boundary layer. This coupling establishes the initial conditions of disturbance amplitude and frequency which eventually grow to create the conditions for the onset of the breakdown of laminar flow and the onset of transition to turbulent flow. As described by Saric et al. [5], receptivity has many paths to introduce a disturbance into the boundary layer, for example the interaction of sound or turbulence with leading-edge curvature or with discontinuities in surface curvature that produces a resonant response in the Tollmien–Schlichting (T–S) boundary layer disturbance waves. Saric et al. [5] further characterize the process as: "Essentially, the incoming freestream disturbance at wavenumber α_{fs} interacts with an inhomogeneity of the body causing its spectrum to broaden to include the response wavenumber α_{TS}. Small initial amplitudes of the disturbances tend to excite the linear normal modes of the boundary layer that are of the T-S type."

Element 2 concerns the disturbance wave structure in the boundary layer flow. In this study, the wave structure is defined with the eigenvalues and eigenfunctions for the laminar boundary layer over a wavy wall, which depend on the background steady flow, accounting for the waviness.

Element 3: The critical feature of the boundary layer disturbances is the wave growth, i.e., whether the wave amplitude increases or decreases with downstream distance. This is calculated by integrating the growth of the disturbances along the streamwise direction, noting that at a given location there is not only local information but also an effect of upstream and downstream conditions.

We show below how elements 1 through 3 are captured using analysis and computations. For elements 4 and 5, once the disturbance waves grow to a level of 0.4% of free-stream velocity, which we refer to as transition onset, a complex sequence of processes occur (three-dimensional linear waves, evolution, and then breakdown of three-dimensional vortical structures, formation of local regions of turbulent flow, or turbulent spots, and finally fully developed turbulence marking the end of transition, at a location where the level of unsteadiness is 3% of free-stream velocity). The criteria developed for onset and the end of turbulence, as well as the length over which the transition takes place, are therefore provided by experiment. They will be described further below, with their measurement and definition seen in Part II. For now, however, it suffices to note the levels and to recognize that *Element 4* defines the conditions for transition onset and *Element 5* defines those for the end of transition.

2.2 Non-Dimensional Parameters and Geometric Regimes. It is useful to define the geometric regimes for wall geometry and disturbance wave behavior, because these determine the type of analysis needed. To start, consider inviscid, incompressible, irrotational two-dimensional flow past an infinite periodic two-

dimensional wavy wall, with parallel uniform flow of velocity U far away from the wall. If the maximum wave height is η, and the wavelength is λ, the only non-dimensional group based on these length scales is the surface wave slope parameter, η/λ.

For wave slope parameter small compared to unity, $\eta/\lambda \ll 1$, the flow perturbations due to the wall are well captured in a linearized description. The governing equation for incompressible, irrotational flow, for example, is Laplace's Equation, $\nabla^2 \varphi = 0$, where φ is the velocity potential, and $\partial\varphi/\partial x = \Delta u$; $\partial\varphi/\partial y = \Delta v$. The disturbance is determined by the boundary condition at the wall and scales with the wall geometry wavelength. The non-dimensional perturbations, such as axial velocity, $\Delta u/U$, and wall pressure coefficient, ΔC_p, are thus sinusoidal with a wavelength, λ, an amplitude proportional to η/λ, and an exponential decay with distance from the surface, y, of $\exp(-2\pi y/\lambda)$ [12,13].

For *boundary layer flow over a wavy surface*, there are additional length scales, and whether the disturbances extend past the boundary layer edge depends on λ/δ where δ is the boundary layer thickness. For $\lambda/\delta \ll 1$, the disturbances due to the wall are contained within the boundary layer and the flow above the boundary layer edge does not feel the existence of surface waviness. If λ/δ is larger than roughly 10, however, the variations reach beyond the boundary layer and the free-stream responds to surface waviness.

To characterize the regime we will address, Fig. 2 shows the geometry divided into four regimes in a λ/δ versus η/λ plane. For regions III and IV, η/λ is less than 0.05, implying the maximum wall slope is small compared to unity and the disturbances are linear. It is noted, however, that there is not a sharp distinction; the value of 0.05, which means that, for $y = \eta_0\exp[2\pi i x/\lambda]$, the maximum slope, $|\partial y/\partial x|_{\max} = 2\pi\eta/\lambda \approx 0.3$ is a conservative value, based on numerical experiments to define the region of applicability [14,15].

For regions I and II, the wall slope is large and the behavior is non-linear [14]. Flow variations due to surface waviness extend outside the boundary layer edge in Regimes I and IV, and are confined inside the boundary layer in Regimes II and III, with the criterion between the two cases approximately $\lambda/\delta \sim 10$ based on an assessment of boundary layer dissipation using edge velocity as described in Ref. [15]. The aerodynamic and geometric regime for the civil composite fans of interest corresponds to Regime III, and the focus of the research is thus linear flow field perturbations inside a wavy wall boundary layer.

3 Methodology Description

3.1 Introduction to the Extended e^N Method.
The methodology that has been created includes analyses of the two-dimensional linear phenomena of boundary layer receptivity and instability and a
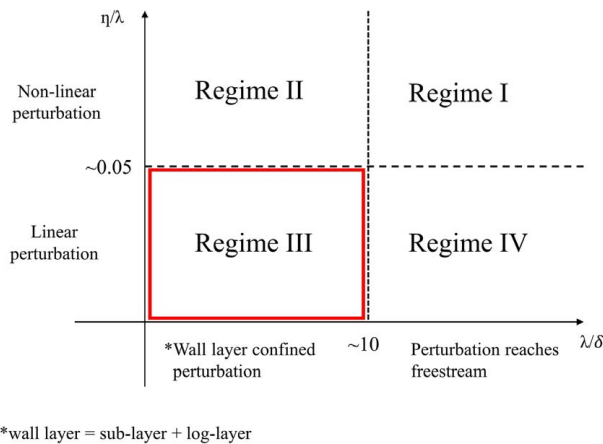
Fig. 2 Geometric regimes—defined based on wall scaling parameter, η/λ, and non-dimensional range of influence, λ/δ. Interest here, for civil composite fans, is Regime III.

simplified transition model to capture the nonlinear processes between onset and end of transition. The analyses comprise two major extensions of an existing approach known as the e^N method [9,16,17], in which the basic idea is to trace the exponential growth of unsteady boundary layer disturbances [18,19] that evolve to transition onset. The first of the two new features is the computation of initial disturbance amplitude using *distributed receptivity analysis*. The second is the capability to capture flow over a wavy surface, i.e., the boundary layer instability is that for the flow over a wavy surface. Neither of these has been previously addressed.

In the original e^N method, the unstable spatial eigenvalues of the Orr–Sommerfeld equation were integrated to obtain an instability growth curve, with disturbances modeled as growing from a common amplitude set by receptivity at the leading edge. Transition onset location was assumed to occur where the wave grows to an empirical criterion, designated as $e^{N_{crit}}$. This method was successful in describing various natural transition scenarios [9,16,20–23].

In the present method, which we refer to as the extended e^N method, the kinetic energy of a Tollmien–Schlichting (TS) wave at a given chordwise location is expressed as the summation of three effects: (i) acoustic forcing, (ii) receptivity at branch I, the location beyond which the TS wave becomes unstable for a given frequency, and (iii) exponential growth of TS waves. The coupling between the effects can be written as in Eq. (1) where U is the boundary layer edge velocity, u_{TS} is the TS wave amplitude, u_{ac} is the root-mean square acoustic fluctuation, and $u_{TS,I}$ is the TS wave amplitude at location I, the location beyond which the growth rate of the instability waves becomes positive. The term location I implies the condition at which the disturbance wave behavior changes from decaying to growing, corresponding to encountering a behavior at which there is a change from one branch of the stability curve to another, denoted by branch I. The notation thus keep consistency with that in the transition community.

$$\log\left(\frac{u_{TS}}{U}\right) = \log\left(\frac{u_{ac}}{U}\right) + \log\left(\frac{u_{TS,I}}{u_{ac}}\right) + \log\left(\frac{u_{TS}}{u_{TS,I}}\right) \qquad (1)$$

In the following sections, we present the modeling of the acoustic receptivity coupling coefficient followed by discussion of wavy wall effects on boundary layer stability, the instability energy integration method, and the description and assessment of the criteria for transition onset, spatial extent and end.

3.2 Receptivity-A: Distributed Receptivity.
A length scale conversion is essential for acoustic receptivity estimation because of the length scale mismatch between acoustic and TS waves. Saric et al. [5] described that

> "The instability waves have phase speeds that are a fraction of the free-stream speed. The energy for naturally occurring freestream disturbances is concentrated at wavenumbers significantly different than the instability wavenumber. Therefore natural receptivity mechanisms require a wavelength conversion process."

In this study, the required length scale conversion is achieved through the spatial non-uniformity of the boundary layer.

The non-localized nature of surface roughness and waviness means that *distributed receptivity theory* [24] is appropriate for the extended e^N method. The receptivity coupling coefficient ($C = u_{TS,I}/u_{ac}$) can be computed following [24] as

$$C = \sqrt{\frac{2}{iD_\alpha}} \frac{\Lambda_\theta}{\sqrt{Re_{x_I}}}$$
$$\int_0^\infty \exp\left(-\frac{\theta_I^2(\alpha_w - \alpha_{TS,I})^2}{iD_\alpha}\right)\left[Re_c \frac{\hat{y}_w(\alpha_w)}{c}\right]d\alpha_w \qquad (2a)$$

$$D_\alpha = 2\left[\theta^2 \frac{d\alpha_{TS}}{dx}\right]_{x_I} \qquad (2b)$$

In Eq. (2b), D_α and $\alpha_{TS,I}$ can be found from the solution of the Orr–Sommerfeld equation. Λ_θ is a modified receptivity efficiency factor and $\hat{y}_w(\alpha_w)$ is the spectral density of surface geometry at wave number of α_w. The receptivity efficiency factor, Λ_θ, of 0.09 was used for the *extended e^N method* because Λ_θ varies from 0.093 to 0.087 for Blasius boundary layer at $Re_{x,I}$ of $0.25 \times 10^6 \sim 2 \times 10^6$ [24].

The receptivity coefficient in Eq. (2b) can be understood as three effects: a proportionality constant, a Gaussian filter based on the surface wave number difference from the TS wave number, and the spectral density of the surface irregularity. The Gaussian filtering means that only a narrow band (with wave number bandwidth $\sim \sqrt{-i[d\alpha_{TS}/dx]_{x_I}}$) of spectral surface irregularity, $\hat{y}_w(\alpha_w)$, contributes.

Figure 3 shows the receptivity coupling coefficient, C, as a function of the non-dimensional wave number $(\alpha_w - \alpha_{TS,I})/\alpha_{TS,I}$, the difference between wall wave number, α_w, and TS wave number at location I, $\alpha_{TS,I}$. The blue line is Eq. (2b), and the red symbols from the measurements of [25]. The coupling coefficient is a maximum when the TS wave number is equal to the wall wave number.

3.3 Receptivity-B: Distributed Receptivity for Spatially Inhomogeneous Surfaces.

The distributed receptivity model (Eq. (2b)) is derived based on a spatially homogeneous surface, for which a single surface spectrum can be defined regardless of location. For spatially inhomogeneous surfaces as in fan geometries, we need to define a way to construct a physically consistent spectrum for receptivity analysis.

Figure 4(a) shows a spatially homogeneous surface for which a single surface wave spectrum, $\hat{y}_w$ in Eq. (2b), can be defined universally along the chord. Suppose, however, that part of the surface is non-wavy, as in Fig. 4(b). A local surface spectrum needs to account for the receptivity variation along the chord. Although a length scale of receptivity variation is not provided in the distributed receptivity model, we can define a physically consistent length scale, or *window*, for receptivity analysis for spatially inhomogeneous surfaces using the TS wavelength, because the receptivity of a TS wave occurs due to surface irregularity over this length scale. We thus define the window size, and the receptivity coordinate characterizing the local geometric power spectrum, based on the TS wavelength.

It is useful to view the local receptivity process at each chordwise location as a boundary value problem based on the inhomogeneous
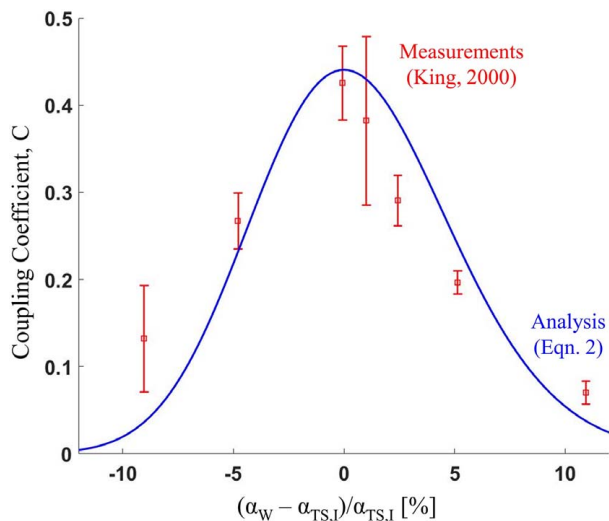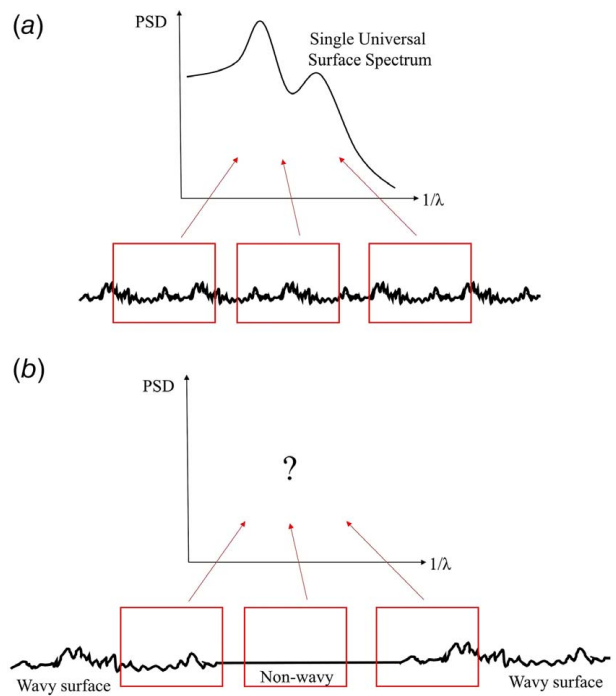
Fig. 4 Motivation of weighted sliding window for spatially inhomogeneous surface: (a) spatially homogeneous surface and (b) spatially inhomogeneous surface

Orr–Sommerfeld equation with acoustic forcing. The receptivity at location I is affected by the local receptivity process, both upstream and downstream, even though the receptivity coupling coefficient ($C = u_{TS,I}/u_{ac}$) focuses only on the TS wave amplitude at location I.

The disturbance due to the local boundary layer forcing upstream of location I decays exponentially until location I. The local receptivity process downstream of location I also affects the overall receptivity, which implies that upstream influence, through pressure disturbances, must be accounted for to describe the behavior upstream of location I.

The effective surface spectrum for receptivity analysis at location I can, therefore, be constructed by ensemble-averaging local spectra based on a sliding window with the TS wavelength scale as in Fig. 5. Figure 5(a) shows a spatially inhomogeneous surface where the local surface spectrum varies along the chord. The receptivity process at location I can be expressed using an *effective surface spectrum* with a weighting function based on exponential decay as in Fig. 5(b). The effective surface spectrum is thus
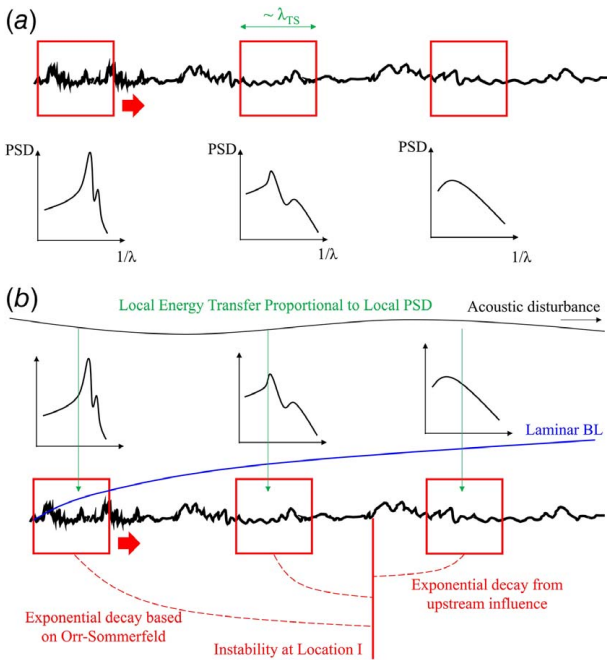
$$\overline{\hat{y}}_w(x_I, \lambda_{TS,I}; F) = \frac{\int_0^{x_I} \hat{y}_w(\xi, \lambda_{TS,I}) W(\xi, x_I; F) d\xi}{\int_0^{x_I} W(\xi, x_I; F) d\xi} \quad (3a)$$

$$W(\xi, x_I; F) = \begin{cases} \exp\left[\int_\xi^{x_I} -\alpha_i(x; F) dx\right] & \text{if } \xi \leq x_I \\ \exp\left[-\left(\frac{\xi - x_I}{4\lambda_{TS}}\right)\right] & \text{if } \xi > x_I \end{cases} \quad (3b)$$

$$F = \frac{\omega \nu}{U^2} \quad (3c)$$

In Eq. (3), $\hat{y}_w(\xi, \lambda_{TS,I})$ is the local spectrum from the sliding window at ξ and window size $\lambda_{TS,I}$. The weighting function $W(\xi, x_I; F)$ always lies between zero and unity.

The sliding window size scale factor and the upstream influence scale factor were determined based on the measured TS waves [26] for the non-wavy surface, to assess leading edge receptivity, and for the wavy surfaces with different waviness onset locations, to assess upstream influence from downstream waviness:

Fig. 3 Experimental validation of receptivity model—blue line, receptivity analysis from Eq. (2b), red symbols, measurements of King [25]

Fig. 5 Definition of effective spectrum for receptivity analysis at spatially inhomogeneous surface using weighted sliding window (Eq. 3). (a) Sliding window with window size based on Tollmien–Schlichting wavelength and (b) effective surface spectrum based on weighted sliding window method.

- Sliding window size scale factor: 4 [Window Size $= 4 \times \lambda_{TS,I}$]
- Upstream influence scale factor: 4

$$W(\xi, x_I; F) = \exp\left[-\left(\frac{\xi - x_I}{4\lambda_{TS}}\right)\right]$$

3.4 Velocity Perturbations for Flow Over a Wavy Wall: Linearized Navier–Stokes Analysis. The linearized Navier–Stokes equations (LNS) are used to describe the flow field variations, and resulting boundary layer destabilization, due to surface waviness. The linearization is that of flow variation with respect to wall slope, in the geometric regime III, as in Fig. 2.

The approach taken is to trace the flow variation at the same distance from the wall as in the non-wavy situation thus correcting the displacement of the wavy wall geometry [27]. We thus solve for the corrections, e.g., $\Delta u(y) = u_{wavy}(y + y_{wavy}) - u(y)$, as in Fig. 6. The LNS are derived in Appendix A.

3.5 Local Stability and Orr–Sommerfeld Equations for Wavy Wall Flow. In the extended e^N method, the eigenvalues are found from a boundary layer stability analysis using the Orr–Sommerfeld equation (see Appendix B) based on the boundary layer velocity profile found from the LNS calculations. The equation can be discretized using a Chebyshev polynominal expansion following [28] and the generalized decomposition method [29] is
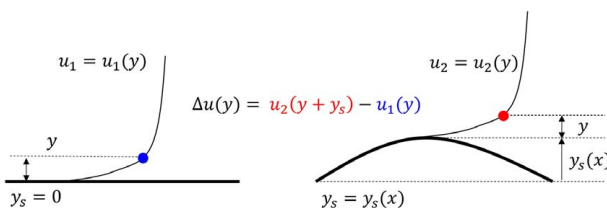
Fig. 6 Wall Corrected Variations—the key idea of LNS is to trace the wall corrected variations

then applied to solve the linear temporal eigenvalue problem. This sets the initial condition for the Newton–Raphson iterations to find the spatial eigenvalues.

3.6 Criteria for Transition Onset, Spatial Extent, and End. The model for the transition process is based on casting the process as the following three steps:

(1) *Transition onset* is initiated once the TS wave amplitude reaches a root-mean-square level of 0.4% compared to the freestream velocity: $u_{TS}/U = 0.4\%$.
(2) The *end of transition* has a constant root-mean-square disturbance level compared to the freestream velocity: $u_{TS}/U = 3\%$.
(3) The *extent of the transition* process is five times the wavelength of the most prominent, in terms of spectral energy density, TS wave at transition onset.

The modeling parameters were set based on the experimental measurements, described in Sec. 3.7.

3.7 Evaluation of Transition Criteria. The descriptions of disturbance growth and evolution have, up to now, been in terms of analysis and computation. This suffices to take us to the onset of transition, which, as mentioned in Sec. 2, brings a much greater level of complexity in the fluid dynamic processes. To describe transition onset, extent, and the disturbance levels, therefore, we make use of the new experimental findings that form a major portion of Part II. We take the step of presenting these here, before recounting the experiment design and operation, because the results form essential features of the natural transition process, and it seems important to present the whole so the reader can see both the context and the quantitative behavior of the separate elements. It is emphasized, however, that the justification of the experiment background and techniques, plus additional experimental findings, are laid out in depth in Part II.

We start by contrasting the features of the disturbance amplitude spectrum upstream and downstream of transition onset. Transition onset is marked by a qualitative change in the disturbance power spectrum. To illustrate the change, Fig. 7 shows the measured velocity disturbance power spectrum as a function of frequency, for the conditions noted in the caption, upstream and downstream of transition onset. The different curves and colors correspond to different values of streamwise locations along the chord.

In Fig. 7(*a*), upstream of onset, the power spectrum is set by a dominant peak that is associated with the Tollmien–Schlichting waves, with the peak is evident at all locations shown. In Fig. 7(*b*), downstream of transition onset, however, we see that there is an evolution to a broadband turbulent spectrum. The start of this evolution occurs at approximately 70% chord for the conditions shown.

Figure 7 does not indicate the disturbance level, but the measurements show (as will be described subsequently) that the disturbance amplitude level at which this change in spectrum occurs is 0.4% for all conditions examined. We thus take this disturbance level as criterion for transition onset.

Measurements for a range of aerodynamic and geometric parameters show that the disturbance amplitude does not grow beyond 3%, and this is taken as indicating the disturbance level at the end of transition [26]. The spatial extent of the transition process between onset and end, is observed to have a length of five times the most prominent wavelength of TS wave at transition onset, in terms of spectral energy density. Figure 8 shows the measured extent of the transition process as a function of the non-dimensional TS wavelength, with the dashed line indicating the proposed approximation. The difference between the approximation and the measurement is within 5% chord, which is the measurement resolution of transition location.
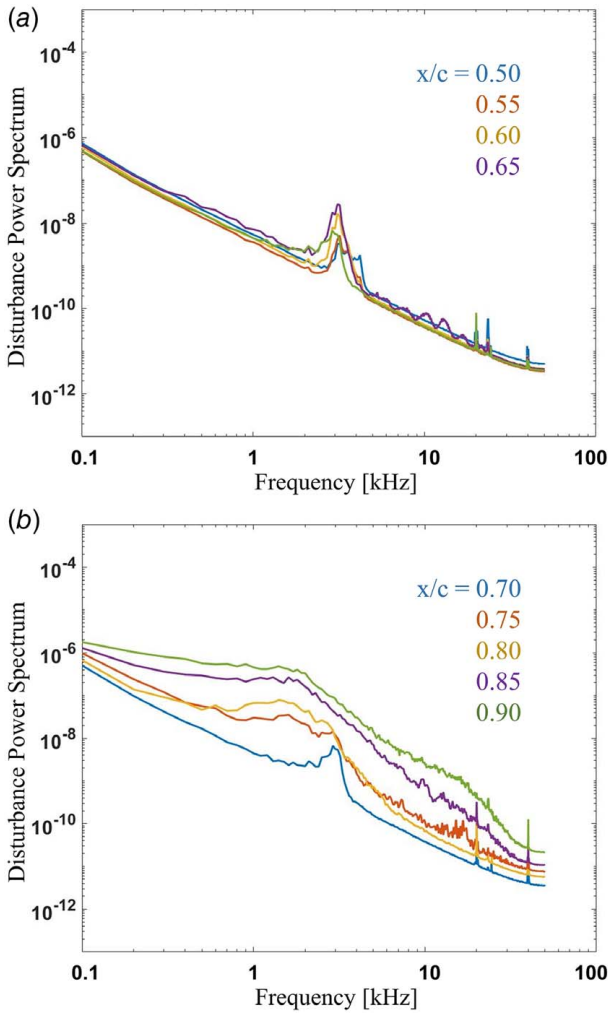
Fig. 7 Evolution of disturbance power spectrum—measured velocity disturbance power spectrum (a) upstream and (b) downstream of the transition onset: $dC_P/d(x/c) = 0.1$, $Re_c = 2 \times 10^6$ [26]
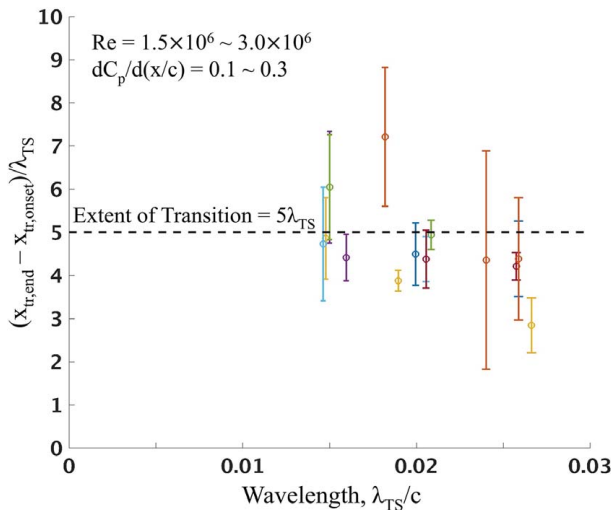
Fig. 8 Measured extent of transition process for a range of aerodynamic conditions—dashed line is approximation of five times predominant TS wavelength at transition onset [26]

4 Physical Interpretation of the Methodology

To determine the total energy of the TS waves, we need to integrate the spectral contributions from all frequencies. This requires us to couple the stability analysis to the transition model. The procedure to achieve this is as follows.

(1) The root-mean-square energy of the acoustic forcing is decomposed into spectral energy components, $\hat{k}_{ac}(\omega)$.

$$E_{ac} = \lim_{T \to \infty} \frac{1}{T} \int_0^T \left[\frac{1}{2} u_{ac}(t)^2 \right] dt = \int_0^\infty \hat{k}_{ac}(\omega) d\omega \quad (4)$$

(2) The spectral velocity $\hat{u}_{ac}(\omega)$ is defined for each frequency of acoustic forcing $\hat{k}_{ac}(\omega)$ as

$$\hat{u}_{ac}(\omega) = \sqrt{2\hat{k}_{ac}(\omega)} \quad (5)$$

(3) The spectral velocity of the TS wave at location I is computed in terms of the receptivity coupling coefficient, $C_{\text{receptivity}}$,

$$\hat{u}_{TS,I}(\omega) = C_{\text{receptivity}} \hat{u}_{ac}(\omega) \quad (6)$$

(4) The growth rate of the spectral velocity for each frequency is

$$\frac{d\|\hat{u}_{TS}(x, \omega)\|}{dx} = -\alpha_i(x, \omega) \quad (7)$$

In Eq. (7), the imaginary part of the spatial eigenvalue, α_i, is the spatial growth rate found from the Orr–Sommerfeld equation.

(5) The relation between spectral velocity and spectral energy is

$$\hat{k}_{TS}(x, \omega) = \frac{1}{2} \hat{u}_{TS}(x, \omega)^2 \quad (8)$$

(6) The total energy of the TS waves at a given chordwise location is obtained by integrating over the different frequencies. The procedure is indicated in Fig. 9 which shows the disturbance energy along the chord. The black dashed line in Fig. 9 shows the initial amplitudes of TS waves which
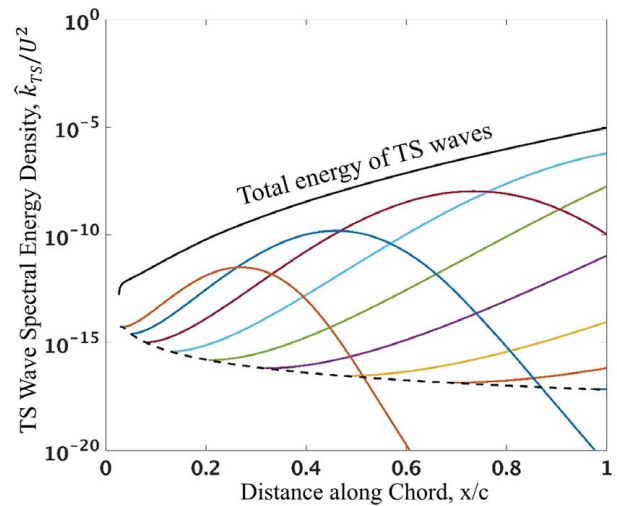
Fig. 9 Exponential Growth of Tollmien–Schlichting Waves—colors indicate different frequencies, dashed line sets initial amplitude from receptivity model. Blasius boundary layer. $Re_c = 4 \times 10^6$.

are set by the receptivity model. The TS waves for various frequencies are represented by the colored lines, and the total energy is shown by the black solid line. With $\hat{k}_{TS}$ the spectral energy density of the TS waves at a given frequency,

$$E_{TS}(x) = \int_0^\infty \hat{k}_{TS}(x, \omega)d\omega \qquad (9)$$

(7) The root-mean-square disturbance velocity, profile is reconstructed from the most unstable eigenmode, $Y_{TS}(x, y)$, of the TS wave. Figure 10 shows the disturbance profiles at different chordwise stations which has the second velocity disturbance peak located near $y/\theta = 5$.

$$u_{TS}(x, y) = Y_{TS}(x, y)\sqrt{2E_{TS}(x)} \qquad (10)$$

(8) The transition onset location is identified as the location at which the boundary layer disturbance, $u_{TS}|_{y/\theta\sim5}$, reaches 0.4% as in Eq. (11). The onset criterion was inferred from measurements of the second velocity disturbance peaks, located near $y/\theta = 5$, because the first peak predicted by theory could not be reached due to hotwire wall contact limitations [26].

$$\left[\frac{u_{TS}|_{y/\theta\sim5}}{U}\right]_{x_{tr,onset}} = 0.4\% \qquad (11)$$

(9) The spatial extent is approximated as proportional to the most prominent wavelength of the TS waves at the onset location in terms of spectral energy density, as in Fig. 8. This implies

$$\Delta x_{tr,process}(\equiv x_{tr,end} - x_{tr,onset}) \approx 5 \times \lambda_{TS} \qquad (12)$$

(10) The spatial extent of the transition process is set by the 3% measured disturbance level at the end of transition.

$$\left[\frac{u_{TS}|_{y/\theta\sim5}}{U}\right]_{x_{tr,end}} = 3\% \qquad (13)$$

5 Complete Model for Natural Transition

Items 1 through 9 in the previous section give the different steps that have been integrated to provide a quantitative description of the natural transition process. To demonstrate the capability, and give
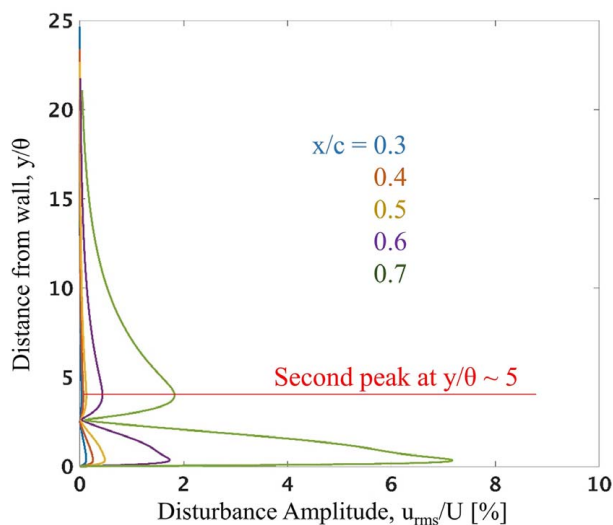
Fig. 10 Profile of Tollmien–Schlichting wave instability eigenmodes at different chordwise stations
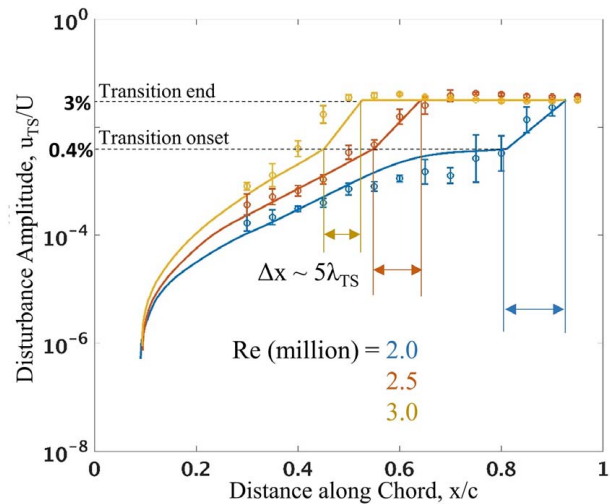
Fig. 11 Transition process—extended e^N analysis with transition model (solid lines) captures experimental measurements (symbols) [26]. Non-wavy surface, $dC_p/d(x/c) = 0.1$.

substance to the comments about mechanism in Sec. 6, we now show measurement results for the non-wavy surfaces (other wavy results are given in Part II). Figure 11 thus shows the boundary layer disturbance amplitude, u_{TS}/U, as a function of distance along the chord, for flow over a non-wavy surface at three different Reynolds numbers. The conditions are given in the caption. Measured spectrum of the external acoustic disturbances and the surface roughness were used as input. The results of the extended e^N methodology are given by the different solid curves and the measurements [26] are indicated by the symbols. Also marked in the figure are the amplitudes for onset of transition and end of transition (the horizontal lines at 0.4% and 3.0% respectively) and the extents of the transition region for the three Reynolds numbers. Both data and model show a change in slope at the transition onset location and a notable marked flattening of the disturbance amplitude at the proposed end of transition for the three values of Reynolds number; the methodology that has been developed captures the observed behavior.

## 6 Changes in Transition Onset Location: Physical Mechanisms

The findings from the extended e^N methodology show that transition onset location is altered on a wavy surface compared to a non-wavy surface because of two independent mechanisms: (i) the receptivity is increased through the interaction between the surface wavelength and the TS waves and (ii) the boundary layer is destabilized through the series of accelerations and decelerations associated with the waviness. In this section, we use the methodology to show that, for fan aerodynamic parameters, the former effect is more important than the effect of boundary layer destabilization. Below, acoustic noise and the surface roughness inputs are used for extended e^N method analysis based on the representative conditions for fan blade operation:

$$\overline{u_{ac}}/U = 10^{-3}$$
$$R_a/c = 2.5 \times 10^{-6} \qquad (14)$$

where R_a is centerline averaged roughness height. It is noted that $Re_{R_a} \ll 100$ and thus the surface is hydraulically smooth [30].

Figure 12 shows the effect of surface waviness on transition boundary layer disturbance growth. The abscissa is the non-dimensional distance along the chord, x/c, and the ordinate is u_{TS}/U, the amplitude of TS disturbance divided by freestream velocity.
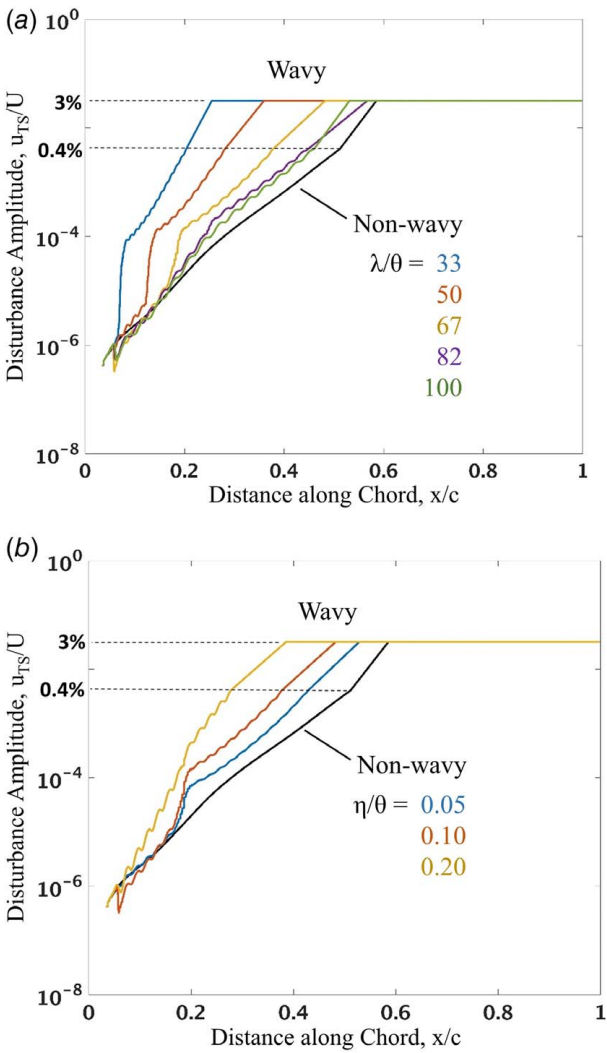
Fig. 12 Effect of geometric parameters on receptivity amplification—$Re_c = 4 \times 10^6$, $dC_p/d(x/c) = 0.1$, $H = 2.48$, $\eta/c = 3.0 \times 10^{-5}$, $X_{w,onset}/c = 5\%$: (a) effect of surface wavelength, λ/θ and (b) effect of surface wave height, η/θ

Figure 12(a) shows the receptivity amplification—the increase of receptivity coefficient and thus of initial amplitude of disturbance waves in the boundary layers due to geometric resonance between surface wavelength and TS wavelength—at different locations along the chord. The different colors denote the ratio of wavelength to boundary layer momentum thickness, λ/θ. The boundary layer momentum thickness, θ, is used instead of boundary layer thickness, δ, as length scale of the velocity profile which is more relevant to discussion of stability.

Receptivity amplification occurs at 5% chord for the blue line, $\lambda/\theta = 33$, and at 20% chord for the yellow line, $\lambda/\theta = 67$. The receptivity amplification occurs when the TS wavelength matches the surface wavelength and it scales linearly with surface wave height. The location of receptivity amplification thus occurs further downstream for the longer non-dimensional surface wavelengths because the TS wavelength grows along the chord as the boundary layer thickens. The wiggles in the disturbance amplitude along the chord are the effect on local boundary layer stability from the series of local acceleration, on crests, and deceleration, on troughs.

Wavy geometries destabilize a boundary layer, i.e., give rise to faster disturbance growth rate, as the non-dimensional wave height, η/θ, increases, as in Fig. 12(b) which shows the growth for different ratios of surface wave height to momentum thickness,

η/θ. Increasing the surface wave height increases the disturbance amplitude, due to receptivity amplification at x/c of 0.2, as shown by the blue line, $\eta/\theta = 0.05$, and the red line, $\eta/\theta = 0.10$. At the largest surface wave height examined, the yellow line with $\eta/\theta = 0.20$, the strong boundary layer destabilization overwhelms the effect of receptivity amplification. Boundary layer destabilization can be mitigated by increasing the non-dimensional surface wavelength, λ/θ, for a fixed non-dimensional wave height.

The effect of boundary layer destabilization and receptivity amplification is exhibited in Fig. 13. The abscissa is non-dimensional wavelength, λ/θ, and ordinate is the normalized transition onset location movement, $-\Delta x_{tr}/x_{tr,0}$ with $x_{tr,0}$ the transition onset location for the non-wavy surface. Figure 13(a) shows the transition onset location movement as a function of non-dimensional wavelength for different chord Reynolds numbers. Figure 13(b) shows qualitative trends of transition onset location movement with non-dimensional wave height and with pressure gradient. The estimated transition onset location movement is up to 50% chord.

The effect of Reynolds number on transition onset location movement occurs in two ways: (i) the onset location movement, Δx_{tr}, occurs at shorter surface wavelength for the smaller boundary layer momentum thicknesses that occur at higher Reynolds number and (ii) the original transition onset location, $x_{tr,0}$, on the non-wavy surface occurs further upstream at higher Reynolds number, leaving less distance for the transition onset location to move. The two effects of Reynolds number can be given a unified description in
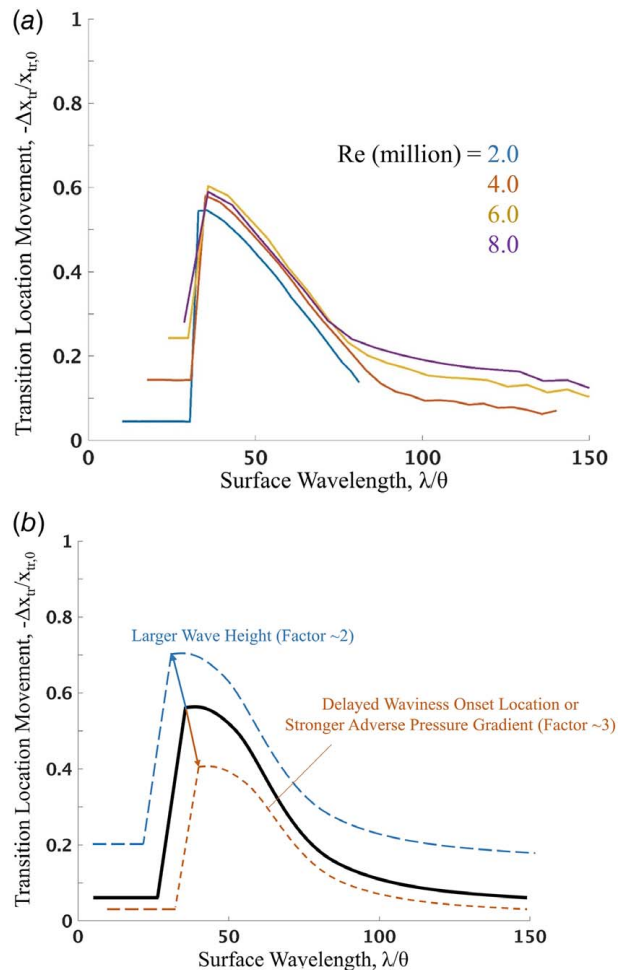
Fig. 13 Effect of surface waviness effects on transition onset location movement—$Re_c = 4 \times 10^6$, $dC_p/d(x/c) = 0.1$, $H = 2.48$, $\eta/c = 3.0 \times 10^{-5}$, $X_{w,onset}/c = 5\%$: (a) effect of Reynolds number and (b) effect of different aerodynamic and geometric conditions

terms of non-dimensional wavelength, λ/θ, and non-dimensional transition onset location movement, $-\Delta x_{tr}/x_{tr,0}$, as illustrated by the solid lines for different Reynolds numbers in Fig. 13(a).

For the range of Reynolds numbers examined, transition onset location movement was most significant for surface wavelength of approximately 40 momentum thickness (or: 40θ), where the effect of receptivity amplification on transition was dominant compared to that of boundary layer destabilization.

The effect of surface waviness on transition onset location movement reduces for stronger adverse pressure gradients because the boundary layer disturbance grows faster than with weaker pressure gradient. For example, increasing $dC_p/d(x/c)$ from 0.1 to 0.2 or 0.2 to 0.3 decreases the non-dimensional transition onset location movement, $-\Delta x_{tr}/x_{tr,0}$, by 0.1. The effect of leading edge shape parameter on the transition onset location movement is weak, less than 0.05 in $-\Delta x_{tr}/x_{tr,0}$, for shape parameter from 2.46 to 2.50.

The transition onset location movement can also be reduced by decreasing the wave height or increasing the location at which surface waviness starts. Decreasing the wave height by factor of 2 decreased the non-dimensional transition onset location movement, $-\Delta x_{tr}/x_{tr,0}$, by 0.2. Increasing the waviness onset location—at which waviness begins—from 5% chord to 10% chord decreased the non-dimensional transition onset location movement, $-\Delta x_{tr}/x_{tr,0}$, by 0.1.

7 Summary

(1) A new integrated methodology has been created to assess the effect of surface waviness on laminar-turbulent transition, and thus profile loss, in civil turbofan carbon composite blades. The natural transition process in these devices, which have no upstream blade rows, is different in kind than the bypass transition in core flow turbomachinery for which the impinging wakes play a major role.

(2) The methodology provides the capability to trace the evolution of disturbance energy transfer in flow over a wavy surface, from its start as external acoustic noise, through exponential growth of Tollmien–Schlichting (TS) boundary layer instability waves, to the start and end of the transition process.

(3) For a given freestream noise level, the initial TS wave amplitude, which sets the boundary layer disturbance wave energy at a downstream station, can be found using an adaptation of distributed receptivity theory, extended to address flow past a wavy wall.

(4) Computations have been carried out of boundary layer perturbations and boundary layer destabilization, due to surface waviness.

(5) The disturbance level growth in the boundary layer is found by integrating the disturbance energy, from all temporal frequencies, along the streamwise direction. The onset of transition is identified as the location at which the boundary layer disturbance amplitudes reach 0.4% of freestream velocity. The spatial extent of transition is found to scale as five times the dominant Tollmien–Schlichting (TS) wavelength. After this length, identified as the end of transition, the disturbance amplitude remains constant at 3% of freestream velocity.

(6) The analysis presented describes, for the first time, the mechanism for the changes in natural transition onset location due to effects of surface waviness. It also shows that the alteration in transition onset location is due to the interaction between geometric waviness and TS boundary layer instability waves. The interaction, and thus the change in onset location, is strongest when the wavelengths of the two quantities are matched.

(7) The computational results presented show the quantitative changes in transition onset due to changes in surface wavelength, surface wave amplitude, and location at which the waviness is initiated on the fan blade. The specific links between transition onset location and blade profile loss are given in Part II, which describes experiments that support the methodology. It will be shown that waviness can result in a decrease of as much as a 1% in fan efficiency.

Conflict of Interest

There are no conflicts of interest.

Nomenclature

c = chord length
$\hat{k}$ = spectral energy
m = surface waviness corrected transformed coordinate along horizontal direction
n = surface waviness corrected transformed coordinate along vertical direction
p = pressure
u = cartesian velocity component in x-direction
$\hat{u}$ = spectral velocity
v = cartesian velocity component in y-direction
x = cartesian coordinate along chordwise direction
y = cartesian coordinate along wall normal direction
C = receptivity coupling coefficient
F = non-dimensionalized Tollmien–Schlichting frequency
H = boundary layer shape parameter
I = branch I: first location beyond which Tollmien–Schlichting wave becomes unstable
U = freestream boundary layer edge velocity
W = weighting function for sliding window
u_{ac} = root-mean-square of acoustic fluctuation
u_{TS} = Tollmien–Schlichting wave amplitude
x_{tr} = transition onset location
$x_{tr,0}$ = transition onset location on non-wavy surface
$\hat{y}_w$ = surface spectrum amplitude
$\overline{\hat{y}_w}$ = effective surface spectrum amplitude
C_p = pressure coefficient
D_α = non-dimensionalized Tollmien–Schlichting growth rate at Branch I
$X_{w,onset}$ = surface waviness onset location: the location beyond which surface waviness exists
Y_{TS} = eigenmode profile of Tollmien–Schlichting wave
E_{TS} = total root-mean-square energy of Tollmien–Schlichting wave
Re_c = Reynolds number based on chord
Re_x = Reynolds number based on chordwise location x
BL = boundary layer
α = Tollmien–Schlichting wave number; $\alpha = 2\pi/\lambda_{TS}$
α_i = imaginary part of Tollmien–Schlichting wave number
α_w = surface wave number
$\alpha_{TS,I}$ = Tollmien–Schlichting wave number at branch I
δ = boundary layer thickness
η = surface wave height
Λ_θ = modified receptivity efficiency factor
λ = surface wavelength
λ_{TS} = Tollmien–Schlichting wavelength
θ = boundary layer momentum thickness
ξ = integration parameter along chord
ν = kinematic viscosity
ω = Tollmien–Schlichting frequency

Appendix A: Derivation of Linearized Navier–Stokes Equations

Tracing the wall corrected variations to linearize the whole computational domain involves a coordinate transformation. The process is to compare the two flow fields, the wavy case and the non-wavy case, in the (flat) transformed domain with the axial, m, and normal, n, direction coordinates. That is,

$$
\begin{aligned}
m &= x \\
n &= y - y_s(x)
\end{aligned}
\tag{A1}
$$

We apply Eq. (A1) to the two-dimensional incompressible continuity and Navier–Stokes equations and neglect higher order terms such as $\Delta u(\partial \Delta u / \partial m)$, resulting in a set of LNS equations. The three unknowns are axial velocity variation, Δu, normal velocity variation, Δv, and pressure variation, Δp, which are functions of m and n.

Applying the transform derivative, $\partial / \partial \xi$, defined as

$$
\frac{\partial}{\partial \xi} \equiv \frac{\partial}{\partial m} - y_s'(m) \frac{\partial}{\partial n}
\tag{A2}
$$

we obtain the set of equations:

$$
\frac{\partial \Delta u}{\partial \xi} + \frac{\partial \Delta v}{\partial n} = y_s'(m) \left[\frac{\partial u_0}{\partial n} \right]
\tag{A3}
$$

$$
\begin{aligned}
u \frac{\partial \Delta u}{\partial \xi} &+ \Delta u \frac{\partial u_0}{\partial \xi} + v_0 \frac{\partial \Delta u}{\partial n} + \Delta v \frac{\partial u_0}{\partial n} + \frac{1}{\rho_0} \frac{\partial \Delta p}{\partial \xi} \\
&- \frac{\mu}{\rho_0} \left[\frac{\partial^2 \Delta u}{\partial \xi^2} + \frac{\partial^2 \Delta u}{\partial n^2} \right] = y_s'(m) \left[u_0 \frac{\partial u_0}{\partial m} + \frac{1}{\rho_0} \frac{\partial p_0}{\partial n} - 2\nu_e \frac{\partial^2 u_0}{\partial m \partial n} \right] \\
&+ y_s'(m)^2 \left[\nu_e \frac{\partial^2 u_0}{\partial n^2} \right] - y_s''(m) \left[\nu_e \frac{\partial u_0}{\partial n} \right]
\end{aligned}
\tag{A4}
$$

$$
\begin{aligned}
u \frac{\partial \Delta v}{\partial \xi} &+ \Delta u \frac{\partial v_0}{\partial \xi} + v_0 \frac{\partial \Delta v}{\partial n} + \Delta v \frac{\partial v_0}{\partial n} + \frac{1}{\rho_0} \frac{\partial \Delta p}{\partial n} \\
&- \frac{\mu}{\rho_0} \left[\frac{\partial^2 \Delta v}{\partial \xi^2} + \frac{\partial^2 \Delta v}{\partial n^2} \right] = y_s'(m) \left[u_0 \frac{\partial v_0}{\partial n} - 2\nu_e \frac{\partial^2 v_0}{\partial m \partial n} \right] \\
&+ y_s'(m)^2 \left[\nu_e \frac{\partial^2 v_0}{\partial n^2} \right] - y_s''(m) \left[\nu_e \frac{\partial v_0}{\partial n} \right]
\end{aligned}
\tag{A5}
$$

where the background flow velocity and pressure, u_0, v_0, and p_0, are predefined, at a given pressure distribution along the chord, from laminar boundary layer analysis. The computed axial velocity profile on the wavy surface, $u_0 + \Delta u$, is then used for the stability analysis as described in Appendix B.

Appendix B: Orr–Sommerfeld Equation

The Orr–Sommerfeld equation describes the behavior of unsteady disturbances in a two-dimensional incompressible boundary layer flow with parallel streamlines. The stability of such flows are defined by the eigenvalues associated with these disturbances. If $u = U(y)$ and $v = 0$ is the known time mean background flow in the boundary layer, the Orr–Sommerfeld equation is obtained by defining a stream function for the disturbance velocities and linearizing the Navier–Stokes equation about the time mean flow [30,31]. The classical form is Eq. (B1).

$$
(\alpha U - \omega)(\hat{\phi}'' - \alpha^2 \hat{\phi}) - \alpha U'' \hat{\phi} + iRe^{-1}(\hat{\phi}'''' - 2\alpha^2 \hat{\phi} + \alpha^4 \hat{\phi}) = 0
\tag{B1}
$$

In Eq. (B1), $\hat{\phi}$, α, and ω are the non-dimensional flow perturbation mode, spatial eigenvalue, and temporal eigenvalue, respectively. The quantities U and U'' are the known time mean velocity and

its second derivative; these include the velocity differences due to wall waviness, as discussed in Sec. 5.

References

[1] Solomon, W. J., and Walker, G. J., 2000, "Incidence Effects on Wake Induced Transition on An Axial Compressor Blade," J. Propul. Power., 16(3), pp. 397–405.

[2] Wissink, J. G., Zaki, T. A., Rodi, W., and Durbin, P. A., 2014, "The Effect of Wake Turbulence Intensity on Transition in a Compressor Cascade," Flow, Turbul. Combust., 93(4), pp. 555–576.

[3] Mayle, R. E., 1991, "The 1991 IGTI Scholar Lecture: The Role of Laminar-Turbulent Transition in Gas Turbine Engines," ASME J. Turbomach., 113(4), pp. 509–536.

[4] White, F. M., 2006, Viscous Fluid Flow, 3rd ed., McGraw-Hill, New York.

[5] Saric, W. S., Reed, H. L., and Kerschen, E. J., 2002, "Boundary-Layer Receptivity to Freestream Disturbances," Annu. Rev. Fluid. Mech., 34, pp. 291–319.

[6] Riedel, H., and Sitzmann, M., 1998, "In-Flight Investigations of Atmospheric Turbulence," Aeros. Sci. Technol., 2(5), pp. 301–319.

[7] Schubauer, G. B., and Skramstad, H. K., 1947, "Laminar Boundary–Layer Oscillations and Stability of Laminar Flow," J. Aeronaut. Sci., 14(2), p. 1947.

[8] Wells Jr., C. S., 1967, "Effects of Freestream Turbulence on Boundary- Layer Transition," AIAA. J., 5(1), pp. 172–174.

[9] van Ingen, J. L., 2008, "The e^N Method for Transition Prediction. Historical Review of Work At TU Delft," 38th Fluid Dynamics Conference and Exhibit, June 23–26, Paper No. AIAA 2008–3830.

[10] Bons, J. P., 2010, "A Review of Surface Roughness Effects in Gas Turbines," ASME J. Turbomach., 132(2), p. 021004.

[11] Winter, K., Hartmann, J., Jeschke, P., and Lahmer, M., 2013, "Experimental and Numerical Investigation of Streamwise Surface Waviness on Axial Compressor Blades," Proceedings of Turbo Expo 2013: Turbine Technical Conference and Exposition, GT2013-95983.

[12] Greitzer, E. M., Tan, C. S., and Graf, M. B., 2004, Internal Flow, Cambridge University Press, Cambridge.

[13] Liepmann, H. W., and Roshko, A., 1957, Elements of Gasdynamics, Wiley, New York.

[14] Esquivelzeta-Rabell, F. M., Figueroa-Espinoza, B., Legendre, D., and Salles, P., May 2012, "Shearing Flow Over An Idealized Wavy Surface: Comparison Between Linear Theory and DNS," 3rd Brazilian Conference on Boiling, Condensation and Multiphase Flow.

[15] Lee, J., 2019, "Characterization and Mitigation of Blade Waviness Effects on Fan Performance," Ph.D. thesis, Massachusetts Institute of Technology, Cambridge, MA.

[16] van Ingen, J. L., 1956, A Suggested Semi-Empirical Method for the Calculation of the Boundary Layer Transition Region. Technical Report.

[17] Reed, H. L., 1996, "Linear Stability Theory Applied to Boundary Layers," Annu. Rev. Fluid. Mech., 28(1), pp. 389–428.

[18] Theofilis, V., 2003, "Advances in Global Linear Instability Analysis of Nonparallel and Three-Dimensional Flows," Prog. Aerosp. Sci., 39(4), pp. 249–315.

[19] Theofilis, V., 2011, "Global Linear Instability," Annu. Rev. Fluid. Mech., 43(1), pp. 319–352.

[20] Seyfert, C., and Krumbein, A., 2013, "Comparison of a Local Correlation-Based Transition Model With An e^N-Method for Transition Prediction," New Res. Num. Exp. Fluid Mech. VIII, 121, pp. 541–548.

[21] Masad, J. A., and Iyer, V., 1994, "Transition Prediction and Control in Subsonic Flow Over a Hump," Phys. Fluids., 6(1), pp. 313–327.

[22] Masad, J. A., 1996, Effect of Surface Waviness on Transition in Three-Dimensional Boundary-Layer Flow. Technical Report.

[23] Boermans, L. M. M., and Blom, J. J. H., 1976, Low-Speed Aerodynamic Characteristics of an 18% Thick Airfoil Section Designed for the All-Flying Tailplane of the M-300 Sailplane. Technical Report, Delft, The Netherlands.

[24] Choudhari, M., 1993, "Boundary-Layer Receptivity Due to Distributed Surface Imperfections of a Deterministic or Random Nature," Theor. Comput. Fluid Dyn., 4, pp. 101–117.

[25] King, R. A., 2000, "Receptivity and Growth of Two- and Three-Dimensional Disturbances in a Blasius Boundary Layer," Ph.D. thesis, Massachusetts Institute of Technology, Cambridge, MA.

[26] Lee, J., Ramaswamy, V., Spakovszky, Z. S., Greitzer, E. M., Drela, M., and Talbotec, J., 2021, "Effects of Surface Waviness on Fan Blade Boundary Layer Transition and Profile Loss—Part II: Experimental Assessments and Applications," Proceedings of ASME Turbo Expo 2021: Turbomachinery Technical Conference and Exposition, Virtual, Online, June 7–11, Paper No. GT2021-58678.

[27] Benjamin, T. B., 1959, "Shearing Flow Over a Wavy Boundary," J. Fluid. Mech., 6(2), pp. 161–205.

[28] Orszag, S. A., 1971, "Accurate Solution of the Orr-Sommerfeld Stability Equation," J. Fluid. Mech., 50(4), pp. 689–703.

[29] Dongarra, J. J., Straughan, B., and Walker, D. W., 2008, "Chebyshev Tau - QZ Algorithm Methods for Calculating Spectra of Hydrodynamic Stability Problems," Appl. Num. Math., 22(4), pp. 399–434.

[30] Schlichting, H., 1979, Boundary Layer Theory, 7th ed., McGraw-Hill, New York.

[31] Panton, R. L., 2013, Incompressible Flow, 4th ed., Wiley, Hoboken, NJ.